Combustion and Flame 257 (2023) 112513

Contents lists available at ScienceDirect

Combustion and Flame

journal homepage: www.elsevier.com/locate/combustflame

HOMO-LUMO energy gaps of complexes of transition metals with single and multi-ring aromatics

Nikolaos Kateris[a], Rui Xu[a,b,c], Hai Wang[a,*]

[a] Mechanical Engineering Department, Stanford University, Stanford, CA 94305, USA
[b] Chemistry Department and The PLUSE Institute, Stanford University, Stanford, CA 94305, USA
[c] SLAC National Accelerator Laboratory, Menlo Park, CA 94025, USA

ARTICLE INFO

Article history:
Received 27 September 2022
Revised 10 November 2022
Accepted 15 November 2022
Available online 15 December 2022

Keywords:
Aromatics
PAH
Organometallic complex
Binding energy
HOMO-LUMO gap

ABSTRACT

Optical and electronic properties of aromatics and their clusters are critical to interpreting phenomena ranging from flame-formed nanoparticles to interstellar dust. These properties are also important to their applications as organic semiconductor materials. Aromatic hydrocarbons often form coordination bonds with metal atoms and cations, forming complexes with electronic properties that differ from their parent aromatics. Metal incorporation to aromatics allows access to a versatile range of optical and electronic properties via the modulation of their band gaps. Here, we investigate the binding of four fourth-row transition metals (titanium, chromium, iron, and nickel) with four aromatic molecules (benzene, naphthalene, pyrene, and coronene), and the HOMO-LUMO energy gap of the metal-aromatic complexes using density functional theory calculations. Neutral and cationic (1+ and 2+) complexes are studied at different geometrical and spin configurations, and their binding energies and HOMO-LUMO gaps are computed for the ground state. It is observed that binding with metals can reduce the HOMO-LUMO gap of the aromatics significantly, and the gap energy of the metal-aromatic complexes is closely correlated with their ionization energy. The number of possible transitions from occupied to unoccupied molecular orbitals was also calculated, showing similar spectral energy features for naphthalene, pyrene, and coronene with and without metal incorporation.

1. Introduction

Carbon nanoparticles (CNPs) are one of the most common carbon allotropes in nature [1]. As a predominantly combustion-formed material, they are of great interest to research ranging from carbon-based materials [2], combustion [1], air pollution [3] to climate change [4]. It is well accepted that flame CNPs nucleate out of polycyclic aromatic hydrocarbon (PAH) precursors and grow in size and mass through a combination of surface reactions and coagulation [5–11]. It has been shown that in typical combustion-formed CNPs, PAH molecules have masses in a range between around 202 amu (which corresponds to pyrene) to over 500 amu. The mean PAH mass is around 300 amu [12–15] (which corresponds to coronene) and the PAHs are typically peri-condensed [16]. Other molecular structures in CNPs may include aliphatics [17–19] and oxygenates [17,20]. Similar PAHs and their existence in the interstellar media were discussed also in a range of astrochemical studies [21–24].

Since the pioneering work of D'Alessio and D'Anna [25,26], it has been well recognized that flame-formed CNPs have well-defined optical band gaps [27–31]. Recent evidence suggests that the ionization energy and optical band gap of CNPs follow closely the quantum confinement behaviors [31]; these properties were found to depend on particle size with smaller particles giving both larger photo-ionization energies and larger optical band gaps. Similar and consistent behaviors have been observed for electronic band gaps [32,33]. The impact of these behaviors on the optical properties of flame CNPs has been discussed recently in the context of light extinction and scattering measurements of soot in flames [34,35]. Theoretical calculations conducted thus far have clearly indicated that the quasi-semiconductor behaviors observed derive largely from the energy gaps between the highest occupied molecular orbital (HOMO) and the lowest unoccupied molecular orbital (LUMO) in PAH molecules, i.e., the molecular building blocks of CNPs [29,36–39]. Studies have also shown that both clustering [31,39,40], and organic and oxygenate functionalizations of PAHs affect their HOMO-LUMO energy gaps [38].

Flame CNPs are multicomponent, inhomogeneous materials [20,41]. As threshold properties related to electron excitation, ion-

* Corresponding author.
E-mail address: haiwang@stanford.edu (H. Wang).

https://doi.org/10.1016/j.combustflame.2022.112513
0010-2180/

ization energy and band gap can be particularly sensitive to specific constituent molecules that have the lowest electron excitation energies [31]. Incorporation of even a small amount of molecules having low excitation energies in CNPs could fundamentally impact their ionization energies and band gaps [39]. To this end, we note that all practical combustion systems contain trace metals with origins ranging from fuel impurity to metal-containing lubricating oils. For example, jet fuels can contain sodium, potassium, aluminum, calcium, magnesium, copper, and iron [42]. It is well known that metal cations may bind strongly and effectively with aromatic molecules typically via π-binding, leading to appreciable binding energies [43–49]. The impact of transition metals on soot nucleation has been studied extensively in the past (see, e.g., [50–52]). There are renewed interests recently in the role of metals on soot formation, including soot mass growth catalyzed by noble and transition metals [53–55], the effects of alkali metal on PAH and soot formation [56,57], and metal-catalyzed soot oxidation (see, e.g., Wang et al. [58], Khaskheli et al. [59]). In addition, metal-aromatic complexes have been of great astrochemical interest. Serra et al. [60] discussed their existence in the interstellar medium as a mechanism for metal scavenging and depletion. Experimental studies explored the reaction of PAHs with iron cations to form organometallic complexes [61,62] and the spectroscopic features of the resulting PAHs ions [23]. Theoretical models were employed to examine the stability [24] and the infrared spectra [63] of Fe-aromatic complexes. In addition, aromatic molecules with atomic substitutions are used as tunable organic semiconductor materials, since their structures can be altered to achieve tunable electronic properties and morphologies of semiconducting films and fibers [64–66]. As importantly, several recent studies used scanning tunneling spectroscopy (STS) to probe the electronic band gap of PAHs and small flame CNPs [32,33]. STS typically uses a transition metal probe on an organic sample immobilized on a gold substrate. Sample contamination due to metal atom transfer to PAH, forming metal-PAH binding, is a distinctive possibility. A basic understanding of the effect of metal incorporation into PAH or flame CNPs is essential to interpreting a STS differential conductance spectrum.

Owing to the high electronic energy density of transition metals, their incorporation into an aromatic molecule or flame formed CNPs is expected to fundamentally alter its HOMO-LUMO gap [67]. Yet, a systematic study of the effect of metal incorporation on the optical properties of PAHs and flame formed CNPs remains unavailable. The overall objective of the current study is to shed light on the effects of transition metal binding on the HOMO-LUMO gap of several model aromatic compounds. For this purpose, we examined molecular complexes of the single-ring aromatic benzene, as well as the polycyclic aromatic hydrocarbons, i.e., naphthalene, pyrene, and coronene with fourth-row transition metals (titanium, chromium, iron, and nickel) using density functional theory (DFT). The complexation of aromatics with metals was investigated over a range of spin multiplicity and oxidation states (neutral and cationic) and binding energies were calculated for the most stable complexes. It will be shown that for the transition metals studied, metal-aromatic complexation leads to an appreciable HOMO-LUMO gap reduction from the parent aromatic without, however, an appreciable change in its energy band structure.

2. Methods

Aromatics (denoted as A_r, r corresponding to the number of six-membered rings) considered in the current study are benzene (C_6H_6, A_1), and polycyclic aromatic hydrocarbons (PAHs) including naphthalene ($C_{10}H_8$, A_2), pyrene ($C_{16}H_{10}$, A_4), and coronene ($C_{24}H_{12}$, A_7). The metal elements considered are titanium (Ti), chromium (Cr), iron (Fe), and nickel (Ni). Fe was selected due to its widespread presence in combustion systems, and Ti, Cr, and Ni provide a sample of fourth-row transition metal elements, both lighter and heavier than Fe. In warm interstellar medium [68] and during fuel combustion [69], high temperatures could lead to many charge and electronic states being accessible. Both neutral and cationic metal-aromatic complexes are investigated for each metal and aromatic combination. The cationic states of the complexes studied are 1+ and 2+, though higher oxidation states could be of interest. Here, we focused only on the 1+ and 2+ charge states because under most relevant gas-phase conditions, available cationic species are expected to be lightly charged due to the significant ionization energy. Furthermore, a variety of spin multiplicities for metal-aromatic complexes needs to be considered. The spin multiplicity of each metal-aromatic complex is dictated by the possible spin multiplicity states of the metal atom. Table 1 lists the spin multiplicities for all the complexes studied herein. Given the four aromatics, four metal atoms, three charge states, two geometric configurations for pyrene and coronene (to be discussed below), and the spin multiplicity states, a total of 210 complexes were calculated.

Table 1
Spin multiplicities considered for all metal-aromatic complexes. The ground-state spin multiplicity of pure metal in each oxidation state is underlined.

	Oxidation state, n		
Complex	0	1+	2+
Ti-A_r^n	1, <u>3</u>	2, <u>4</u>	1, <u>3</u>, 5
Cr-A_r^n	1, 3, 5, <u>7</u>	2, 4, <u>6</u>	1, 3, <u>5</u>, 7
Fe-A_r^n	1, 3, <u>5</u>	2, 4, <u>6</u>	1, 3, <u>5</u>, 7
Ni-A_r^n	1, <u>3</u>	<u>2</u>, 4	1, <u>3</u>, 5

DFT calculations were performed using the unrestricted B3LYP functional [70–72] with the triple-ζ cc-pVTZ basis set [73,74]. The B3LYP functional has been widely used in calculations involving aromatic molecules and has been shown to provide reliable results [38,39,47,75,76]. The cc-pVTZ basis set was selected because of its extensive nature, which includes d and f polarization functions that are important for the heavy transition metal elements involved. In addition, it allows for the consideration of relativistic effects in deep core electrons. All calculations were performed on Gaussian 16 [77]. The sum of electronic and zero-point vibrational energies for each compound studied are compared for each metal-aromatic complex in each charge state, in order to determine the spin multiplicity state that corresponds to the ground state.

Initial geometry guesses were created by placing a metal atom on top of an aromatic ring, as illustrated in Fig. 1. In particular, both the pyrene and the coronene molecules present two different aromatic ring choices for π bindings. For pyrene, a metal atom on top of the two equivalent rings by the centroid of the molecule is called the “inner” configuration hereafter, while an atom on top of the remaining rings is named the “outer” configuration. For coronene, a metal atom on top of the central ring is named the “inner” configuration and that on top of the remaining rings (e.g., ring edge) is named the “outer” configuration. The geometry of each complex was optimized and a frequency calculation followed to ensure that the converged structure is at a potential energy surface minimum. The vibrational frequencies were scaled by the appropriate anharmonic correction factor (0.9612 for the level of theory used [78]).

In the event of calculations yielding complexes with imaginary frequencies, the optimization was relaunched by moving the metal along the reaction coordinate until a stable geometry is achieved. Certain spin multiplicity states (see Supporting Information) did not produce stable complexes, but in all cases, they can be disregarded because of their high electronic energy as compared to the corresponding ground state complexes.

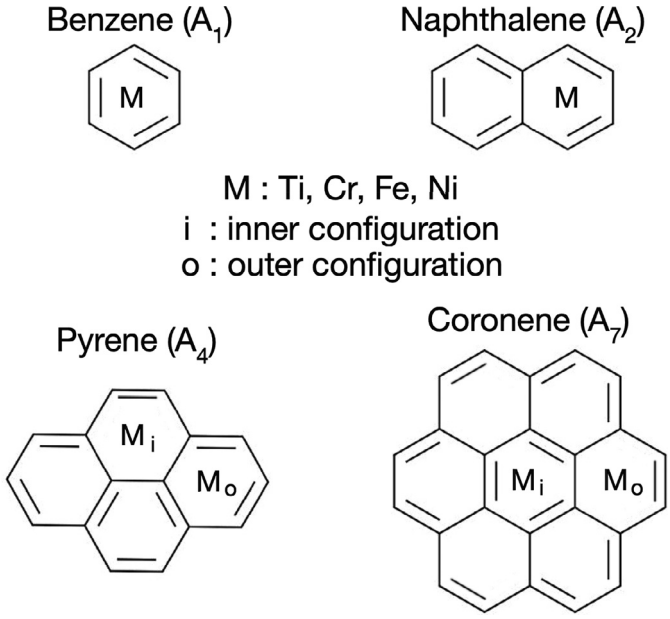

Fig. 1. Schematic of metal-aromatic complexes for benzene, naphthalene, pyrene, and coronene. Metal atoms are positioned on top (or bottom) of aromatic rings. In the cases of metal-pyrene and metal-coronene complexes, the "inner" and "outer" configurations are denoted by the subscripts "i" and "o", respectively.

The binding energy of transition metal atoms to aromatics was calculated for each complex at each charge state. This was determined by comparing the sum of electronic and zero-point vibrational energy of each complex with those of the dissociated products, namely a neutral or charged aromatic and a metal atom or cation, respectively. The appropriate value for the binding energy corresponds to the lowest energy dissociated products, which depend on the way charge is distributed. Therefore, the binding energy for a complex with positive charge n is calculated as follows:

$$E_b = \min_{0\le i\le n}\left\{E_{\mathrm{M}^i} + E_{\mathrm{A}_r^{n-i}}\right\} - E_{\mathrm{M\text{-}A}_r^n}. \quad (1)$$

The binding energy was in addition corrected by the basis set supoerposition error (BSSE), estimated *a posteriori* using the counterpoise method [79]. A positive binding energy thus corresponds to the metal-aromatic complex being more thermodynamically favored than the dissociated products, while a negative binding energy means that the dissociated products are favored over the complex. Only positive charges are considered in the dissociated products, since splitting a positive charge into a larger positive charge and a negative charge would require excessive energy, due to the additional ionization energies and electron affinities that arise.

The Kohn-Sham molecular orbital energies of the ground state complexes were used to determine their energy gaps. The energy difference ($E_{\mathrm{H\text{-}L}}$) between the highest occupied molecular orbital (HOMO) and the lowest unoccupied molecular orbital (LUMO) can be directly calculated from the energy band structure. It has been shown that the B3LYP functional could overestimate the gap size of aromatic compounds in comparison with experimental absorption measurements [76]. Since an exact match should not be expected [80], the B3LYP functional is still considered to be appropriate especially if the objective is to compare the HOMO-LUMO gaps of aromatic compounds. Since high-spin states studied here contain unpaired electrons, HOMO-LUMO gaps are calculated separately for α and β electrons with the unrestricted B3LYP functional. Both $E_{\mathrm{H\text{-}L}}$ values are calculated and the smaller of the two is presented for each complex, as it is the smaller value that determines the energy gap size of the complex.

Experimentally, the optical band gap E_g^{opt} of the related CNP materials can be acquired from UV–vis absorption measurements (see, e.g., Ref. [31]). According to Tauc [81], the optical band gap of a corresponding condensed-phase material may be determined from the absorbance α:

$$\alpha h\nu \propto (h\nu - E_g^{\mathrm{opt}})^k, \quad (2)$$

where h is Planck's constant and ν is the photon frequency. Electronic state calculations may be used to infer the value of k [31,40]. Previously, it was found that the exponent k is close to 2 for PAHs and their clusters. The value is also consistent with those observed experimentally on flame CNPs over a wide range of particle sizes [31].

In order to determine such a power law for absorbance, we assume that $\alpha h\nu$ is proportional to the number of transitions of energy states $n(\Delta E)$ from occupied to occupied molecular orbitals [31,40]:

$$\alpha h\nu \propto n(\Delta E) = \int N_{\mathrm{O}}(E) N_{\mathrm{U}}(E+\Delta E) dE, \quad (3)$$

where N_{O} and N_{U} are the electronic state densities of occupied and unoccupied molecular orbitals, respectively. These electronic state densities are taken directly from the Kohn-Sham orbital energies of the DFT calculation. A problem to circumvent is the fact that DFT is not known to predict degenerate molecular orbitals as having identical energies, because only the total electron density of the molecule is conserved [82]. To overcome this problem and allow N_{O} and N_{U} to take finite values greater than unity, Kohn-Sham eigenvalues are grouped in bins of width equal to 0.5 eV. Provided enough transitions are available, the exponential fit is insensitive to the bin width.

3. Results and discussion

3.1. Geometries and binding energies

Spin multiplicity adds an important dimension of complexity to the identification of the ground state metal-aromatic structures for HOMO-LUMO energy calculations. In addition, the binding energy of a metal-aromatic complex is another parameter important to the highest charge state we must consider. Figure 2 illustrates the ground state selection as determined by the energy of optimized geometries of metal-aromatic complexes, using 4 of the 210 test complexes as examples. They include all aromatics, metals, and charge states considered here. For each complex, the spin multiplicity state with the lowest energy is selected as the ground state, hence the triplet, doublet, quartet, and septet for Fig. 2(a)–(d), respectively. It should be noted that Fig. 2(c) and (d) only show the outer geometric configuration for pyrene and coronene. The same analysis was applied to the inner configuration and the ground state is selected as the lowest energy state of all possible configurations.

Applying the energy analyses, using Eq. (1), to all metal-aromatic complexes at each charge state, the spin multiplicities of the ground states are identified and listed in Table 2, along with the BSSE-corrected binding energies to be discussed later. As it is shown, the metals considered exhibit similar behavior regarding the multiplicity of the most stable complex. For all aromatics considered, titanium complexes in the triplet, quartet, and triplet state are the most stable for the neutral, 1+, and 2+ complexes, respectively. Similarly, Cr complexes are the more in the septet state for the neutral, sextet state at 1+ charge state, and the quintet state at 2+ state. Fe complexes in the quintet, quartet, and quintet states are the most stable for the neutral, 1+, and 2+ complexes, respectively, with the exception of Fe-A_1^0, which is more stable at the

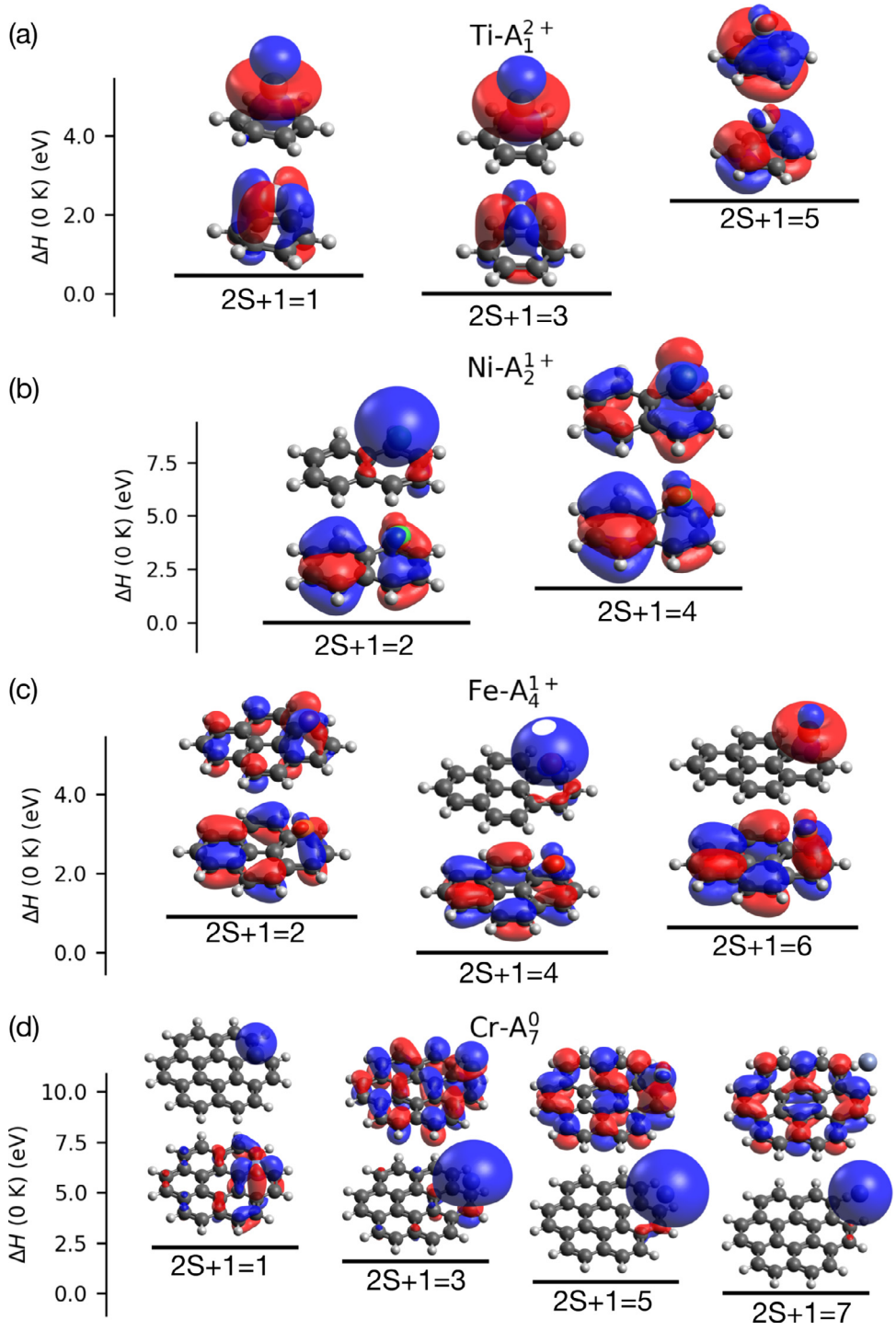

Fig. 2. Relative zero-point corrected electronic energy (in eV) for metal-PAH complexes for different spin multiplicities. The HOMO (lower plot) and LUMO (upper plot) molecular orbital electron densities are included for each multiplicity value. The complexes presented are: (a) Ti-A_1^{2+}, (b) Ni-A_2^{1+}, (c) Fe-A_4^{1+} (outer configuration), (d) Cr-A_7^0 (outer configuration).

triplet state. Ni complexes in the singlet, doublet, and triplet states are the most stable for increasing charge.

The current results are in agreement with those of Simon and Joblin for Fe-PAH complexes [45], who deduced that the quintet state is favored for neutral complexes and the quartet state is favored for 1+ charged complexes. Moreover, we found that for Fe-A_1^0, the triplet state is the ground state (in agreement with calculations by Pandey et al. [83]), having a lower energy than the singlet and quintet states, by 1.67 eV and 0.63 eV, respectively. Our results are in general agreement with calculations for Fe_{1-2}-A_7 by Senapati et al. [48], with the exception of the ground state multiplicity. They stated that the triplet is the ground state for Fe-A_7^0 and that the doublet is the ground state for the 1+ cation. However, these ground states were inferred only from those of the metals without considering the impact of the PAH molecules in the complexes. Our results also match those of Simon and Joblin for the Fe-PAH^{1+} complexes, with the quartet being the ground state for all of the aromatics considered.

Table 2
Binding energies in eV computed for the lowest energy geometric configurations of the metal-aromatic complexes considered and comparison with selected literature values. The value in the parenthesis is spin multiplicity.

Complex	Oxidation state, n						
	0		1+		2+		
					$M^{2+}+A_r^0$		$M^{1+}+A_r^{1+}$
Ti-A_1^n	1.29 (3)	0.96[e]	2.47 (4)[c]	2.68 ± 0.09[f]	4.72 (3)		−0.34
Cr-A_1^n	0.00 (7)	0.12[e]	1.59 (6)[c]	1.76 ± 0.10[f]	6.11 (5)		−1.81
Fe-A_1^n	0.66 (3)	>0.7[e]	2.07 (4)[c]	2.15 ± 0.10[f]	6.51 (5)	5.45–7.42[i]	−0.97
Ni-A_1^n	0.36 (1)	0.87–1.30[e]	2.50 (2)[c]	2.52 ± 0.11[f]	7.93 (3)	7.69–7.85[j]	−1.75
Ti-A_2^n	1.13 (3)		2.47 (4)[c]		6.10 (3)		−0.15
Cr-A_2^n	0.00 (7)		1.71 (6)[c]		7.22 (5)		−1.89
Fe-A_2^n	0.28 (5)	0.64 (5)[g]	2.94 (4)[c]	2.77 (4)[g]	7.47 (5)		−1.21
Ni-A_2^n	0.49 (1)		2.58 (2)[d]		9.23 (3)	8.98–9.25[j]	−1.64
Ti-A_4^n	0.99 (3)[a]		2.57 (4)[a],[c]		6.81 (3)[a]		−0.17
Cr-A_4^n	0.00 (7)[a]		1.86 (6)[a],[c]		8.41 (5)[a]		−1.43
Fe-A_4^n	0.38 (5)[b]	0.68 (5)[g]	2.68 (4)[a],[d]	2.60 (4)[g]	8.82 (5)[a]		−0.59
Ni-A_4^n	0.51 (1)[b]		1.99 (2)[a],[d]		10.58 (3)[a]		−1.02
Ti-A_7^n	0.74 (3)[a]		2.50 (4)[a],[c]	2.26 (4)[h]	6.83 (3)[a]		−0.28
Cr-A_7^n	0.00 (7)[a]		1.85 (6)[a],[d]	2.00 (6)[h]	8.87 (5)[a]		−1.11
Fe-A_7^n	0.30 (5)[a]	0.62 (5)[g]	2.61 (4)[a],[d]	2.59 (4)[g]	9.08(5)[a]		−0.46
Ni-A_7^n	0.43 (1)[a]		1.84 (2)[a],[d]		11.30 (3)[a]		−0.44

[a] Outer configuration as the lowest energy configuration.
[b] Inner configuration as the lowest energy configuration.
[c] Binding energy with respect to $M^{1+}+A_r^0$.
[d] Binding energy with respect to $M^0+A_r^{1+}$.
[e] Estimated from the binding energies of the corresponding 1+ cations and the ionization energy of the neutral complex; see Ref. [83].
[f] Direct measurement; see Ref. [84].
[g] MPW1PW91/6-31+G(d,p) theory from Ref. [45].
[h] B3LYP/6-31G* & 6-311+G* energies on geometry optimized at B3LYP/6-311G & 3-21G level of theories, from Ref. [47].
[i] Range of DFT levels of theory from Ref. [85].
[j] B3LYP, B3LYP-GD3BJ, B3LYP-GD3BJ-BSSE/Stuttgart-Dresden SDD & 6-311++G(d,p) theory, from Ref. [75].

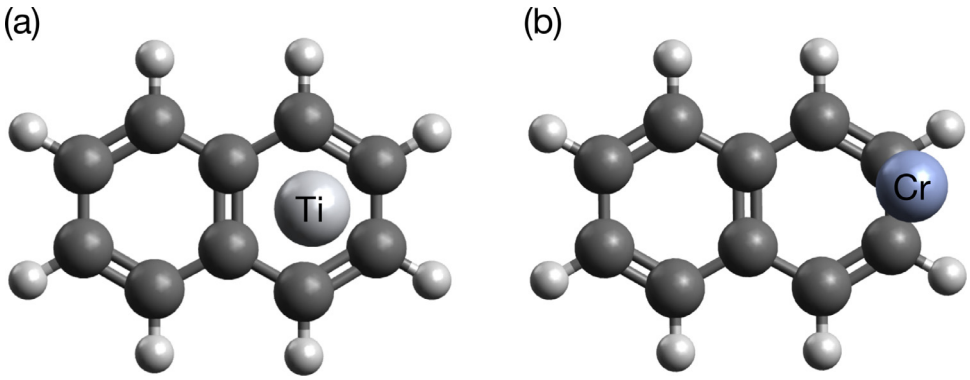

Fig. 3. Optimized structures for (a) Ti-A_2^0 and (b) Cr-A_2^0.

The outer metal-coronene configuration is always favored over the inner configuration (see, Fig. 1); the inner configuration leads to complexes of higher energies, either as a local minimum or a first-order saddle point, or those whose local energy minima cannot be found by the level of theory used (see, the Supporting Information). For the charged pyrene complexes, the outer configuration is found to be always favored. The neutral pyrene complexes differ to an extent, with Fe-A_4^0 and Ni-A_4^0 favoring the inner configuration.

In all of our calculations, the metal atom was initially placed at the center atop a given aromatic, six-membered ring. During geometry optimization of some complexes, the metal atom migrated toward the edge of the aromatic molecule structure. Examples are shown in Fig. 3(b): while the Ti atom stayed near the center of the aromatic ring, Cr migrated to the edge. The edge-π bindings are preferred for neutral Cr, Fe, and Ni complexes with PAHs larger than benzene (with the exception of Ni-A_4^0), as well as for Cr-A_7^{2+} and Ni-A_7^{2+}. This behavior has been reported for Fe-PAH complexes previously [45]. Ti is the only metal considered that consistently stays near the center of an aromatic ring.

Binding energies calculated for each complex at its ground state are listed Table 2. The values include a BSSE correction. For the neutral complexes, the binding energies may be calculated in a straightforward manner, by using the energies of the metal atom and neutral aromatic at their respective ground states. For cationic complexes, however, the binding energy calculation can be more involved. Care must be taken to consider the comparable ionization energies of the transition metal atoms and aromatics. For the 2+ cations, the dissociated products of the lowest respective energies are those with both the metal and aromatic at the 1+ charge state, because of the large second ionization energy of transition metals and aromatics. For example, the second ionization energy of the Ni atom is 18.2 eV (2nd), substantially larger than the first ionization energy at 7.6 eV [86]. Likewise, coronene has the second ionization energy of 12.8 eV and the first ionization energy 7.3 eV [87,88]. Regardless, none of the 2+ complexes are found to be sta-

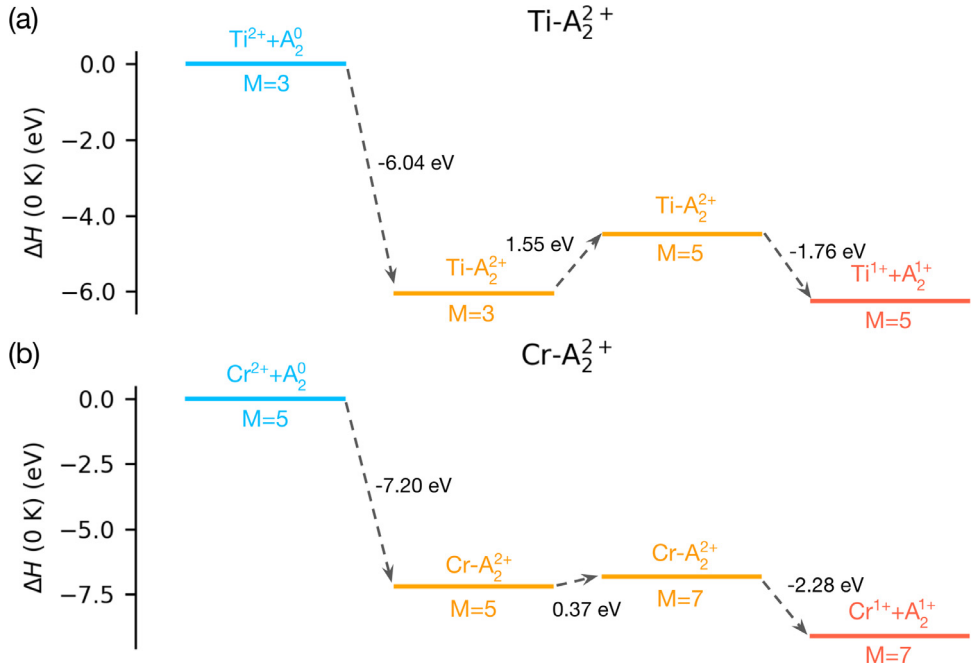

Fig. 4. Enthalpy change at 0 K from a neutral PAH and a 2+ cation (first bar, blue) to the formation of the complex (second and third bars, orange), to dissociation (last bar, red), for (a) Ti-A_2^{2+} and (b) Cr-A_2^{2+}. The total multiplicity (M) of compounds is included.

ble, as the binding energies are all negative (see, the last column of Table 2).

For the 1+ cation complexes, the energies of the dissociated products were evaluated for both M^{1+}+A_r^0 and M^0+A_r^{1+} pairs. The results differ among the complexes considered. Metals in the 1+ cationic state are always favored as the dissociated products from M-A_1^{1+}, because of the large ionization energy in benzene (9.24 eV [89]). The ionization energy of aromatics tends to decrease with their size, and hence, the charge states of the dissociated metals and aromatics begin to differ starting from naphthalene. For instance, the Ti cationic complexes have the lowest binding energies with M^{1+}+A_r^0 assigned as the dissociation products, while the Ni cationic complexes with naphthalene, pyrene, and coronene favor the M^0+A_r^{1+} pair as the dissociated products. These results can be understood again by considering the ionization energy. That is, the first ionization energy of Ni is higher than that of Ti by more than 0.8 eV [86]. For each 1+ cationic complex, the binding energy value listed in Table 2 corresponds to its lowest dissociation energy at 0 K.

The computed binding energies are compared with experimental data, where available, in Table 2. The dissociation energies have been measured experimentally for all the M-A_1^{1+} complexes [84]. The binding energy of a neutral complex may be calculated from that of the corresponding 1+ catonic complex and the ionization energy [83]. As presented in Table 2, good agreement is observed between theory and experiment for all 1+ cationic benzene complexes (to within 0.21 eV); the discrepancy is within 0.33 eV for neutral Ti, Cr, and Fe complexes. Our cationic complex binding energies also agree with previous computational work by Wedderburn et al. [90] (within 0.38 eV), Jaeger et al. [91] (within 0.11 eV), and Yang and Klippenstein [46] (within 0.16 eV).

Our calculations appear to underpredict the binding energy of the neutral Ni-A_1 complex notably. Suffice it to note that the literature values listed in Table 2 were estimated by Pandey et al. [83] from the cation binding energies [84] and the metal-A_1 complex ionization energy [92]. To shed light on the discrepancies, we computed the ionization energy for the complex, and found that the discrepancy can be attributed to, at least partly, to the discrepancy in the ionization energy. Our calculated ionization energy is smaller than the range used in Pandey et al.'s estimate, by 0.25–0.68 eV.

Our binding energies are compared with computed values of the naphthalene, pyrene and coronene complexes in literature, where available. The results are satisfactory, as given in Table 2, in spite of the differences in the levels of theory used, for all cases except for the Fe-A_r^0 complexes, where the largest discrepancy is 0.36 eV compared to the results of Simon and Joblin [45]. The discrepancy is attributed to the large BSSE correction of 0.29, 0.27, and 0.29 eV for naphthalene, pyrene, and coronene, respectively. Other studies also reported the binding energies for some of the complexes studied. They are not listed in the table because the results are not comparable to the current study. For example, Bauschlicher [44] calculated the binding energy of Fe-A_7^{1+}, assuming Fe^{1+}+A_7 to be the dissociation products on the basis of a Mulliken charge analysis of the complex. This differs from our assignment (Fe+A_7^{1+}) based on the calculated ionization energies of Fe and A_7, in agreement with Senapati et al. [48]. We note that our binding energy values are also in close agreement with those of Szczepanski et al. [93] for Fe-A_1^{1+}, Fe-A_2^{1+}, and Fe-A_4^{1+} the 1+ cationic Fe complexes with benzene, naphthalene, and pyrene. Kerkeni et al. [75] reported the binding energy of Ni-A_2^{1+} to be 2.82 eV, higher than our value (2.48 eV). The difference is attributable also to the dissociation product assignment. In addition, Klippenstein and Yang [47] reported the binding energies of Fe-A_7^{1+} and Ni-A_7^{1+}. Their results are excluded from comparison for the same reason. For the Ti-A_7^{1+} and Cr-A_7^{1+} complexes, our binding energies are close to those of Klippenstein and Yang [47], but the agreement is fortuitous to an extent, because the C_{6v} symmetry they imposed on the complex led different complex structures about the metal position. As discussed before, our geometry optimization yielded the outer configuration for both complexes. It should be noted that the counterpoise BSSE correction is small for the majority of complexes (0.01 eV), with some exceptions noted above for Fe-A_r^0, where the BSSE correction is significant, but still smaller than 0.3 eV. This result supports the choice of the cc-pVTZ basis set as an appropriate basis set for this work.

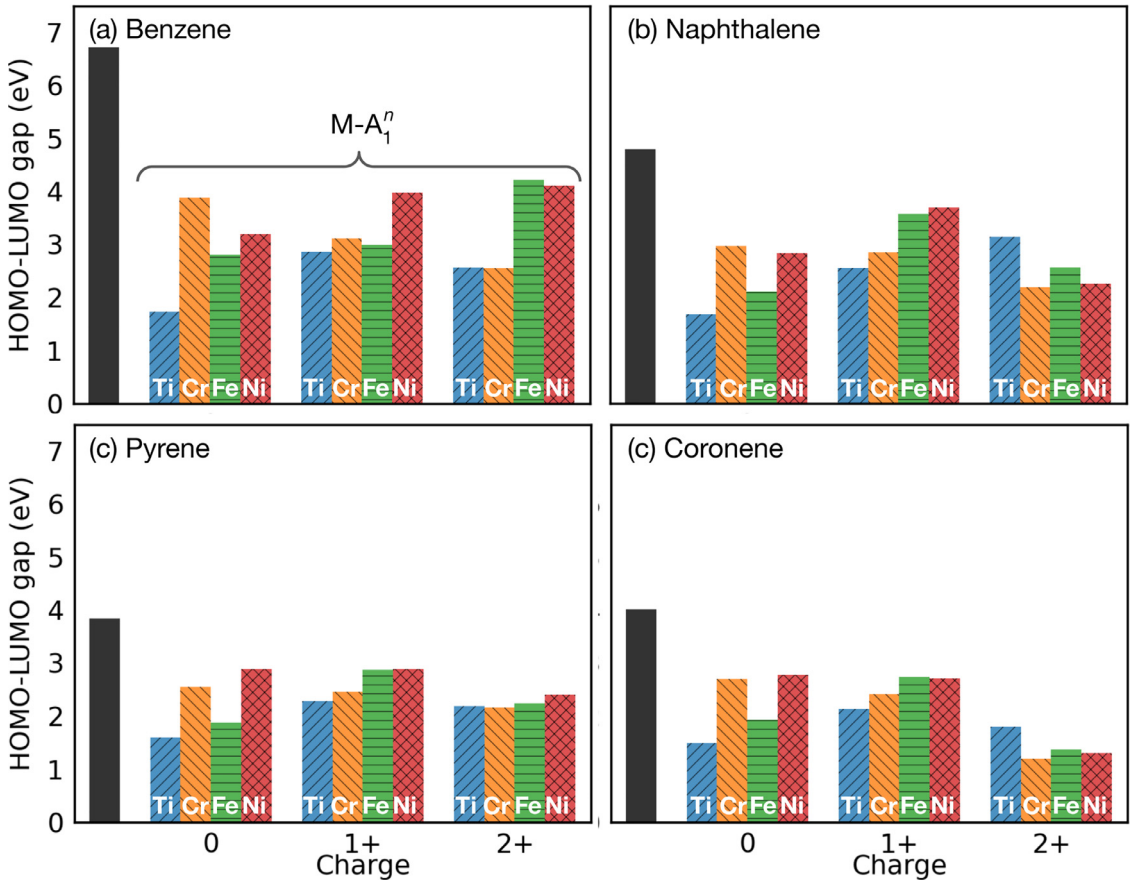

Fig. 5. The HOMO-LUMO gaps of the most stable neutral and cationic metal-aromatic complexes compared with those of the corresponding aromatics: (a) benzene, (b) naphthalene, (c) pyrene, and (d) coronene.

Table 3
HOMO-LUMO energy gap in eV computed for the lowest energy geometries of the metal-PAH complexes considered. The value in the parenthesis is spin multiplicity.

	Oxidation state, *n*		
Complex	0	1+	2+
A_1	6.71		
Ti-A_1^n	1.73 (3)	2.86 (4)	2.57 (3)
Cr-A_1^n	3.88 (7)	3.11 (6)	2.55 (5)
Fe-A_1^n	2.81 (3)	2.99 (4)	4.22 (5)
Ni-A_1^n	3.20 (1)	3.97 (2)	4.11 (3)
A_2	4.79		
Ti-A_2^n	1.68 (3)	2.55 (4)	3.15 (3)
Cr-A_2^n	2.97 (7)	2.85 (6)	2.19 (5)
Fe-A_2^n	2.11 (5)	3.57 (4)	2.56 (5)
Ni-A_2^n	2.83 (1)	3.69 (2)	2.26 (3)
A_4	3.84		
Ti-A_4^n	1.60 (3)[a]	2.29 (4)[a]	2.19 (3)[a]
Cr-A_4^n	2.55 (7)[a]	2.46 (6)[a]	2.16 (5)[a]
Fe-A_4^n	1.88 (5)[b]	2.87 (4)[a]	2.24 (5)[a]
Ni-A_4^n	2.89 (1)[b]	2.89 (2)[a]	2.41 (3)[a]
A_7	4.02		
Ti-A_7^n	1.49 (3)[a]	2.14 (4)[a]	1.80 (3)[a]
Cr-A_7^n	2.70 (7)[a]	2.42 (6)[a]	1.20 (5)[a]
Fe-A_7^n	1.94 (5)[a]	2.74 (4)[a]	1.37 (5)[a]
Ni-A_7^n	2.78 (1)[a]	2.72 (2)[a]	1.31 (3)[a]

[a] Outer configuration as the lowest energy configuration.
[b] Inner configuration as the lowest energy configuration.

Metal cation formation is likely to occur in high-temperature environments. However, elevated temperatures favor dissociation. Therefore, in order to assess the stability of cationic complexes at high temperatures, where metal cations formation is likely, the Gibbs free energy of dissociation has been calculated for Ti-A_4^{1+} and Fe-A_4^{1+} at 298.15 K, 1000 K, and 2000 K as examples. The BSSE-corrected resulting values are 2.20 eV, 1.32 eV, and 0.10 eV for Ti-A_4^{1+} and 2.32 eV, 0.70 eV, and −0.52 eV for Fe-A_4^{1+}, respectively. This shows that both of the selected complexes are more favored over their dissociation products at room temperature and at 1000 K, and Ti-A_4^{1+} is still quite stable at 2000 K.

To understand the preferred position and nature of the metal-aromatic bindings, we performed a natural bond orbital analysis (NBO) on all M-A_2 complexes. As examples, the structures of Ti-A_1^0 and cr-A_1^0 are shown in Fig. 3. We found that the Ti atom forms coordination covalent bonding with the aromatic structure. For example, in Ti-A_1^0, the Ti atom forms 2-center covalent bonds with two C atoms, with occupancies equal to 0.89 and 0.85. The bond orbitals originate from the Ti d-orbital and the C p-orbital. The Ti atom interacts weakly with the remaining carbon atoms, with Wiberg bond indices of 0.28. In contrast, the binding in Cr-A_1^0 is extremely weak: the Wiberg index is 0.0057 between Cr atom and its closest carbon atom; the interactions are even weaker with the remaining carbon atoms in the ring. Fe-A_1^0 and Ni-A_1^0 also exhibit covalent 2-centere bonds of occupancies equal to 0.73 and 0.71, respectively. The stronger coordination bonding in Ti-A_1^0 explains its relatively large binding energy (1.13 eV, see, Table 2), compared to the other neutral complexes. NBO analyses also show that the 2+ cationic complexes form no 2-center bonds, with the exception of one bond in Cr-A_2^{2+} of occupancy of 0.71, involving solely the d-orbital of Cr and the p-orbital of C. These cationic complexes have small Wiberg index values, in agreement with the negative binding energy computed (to be discussed below).

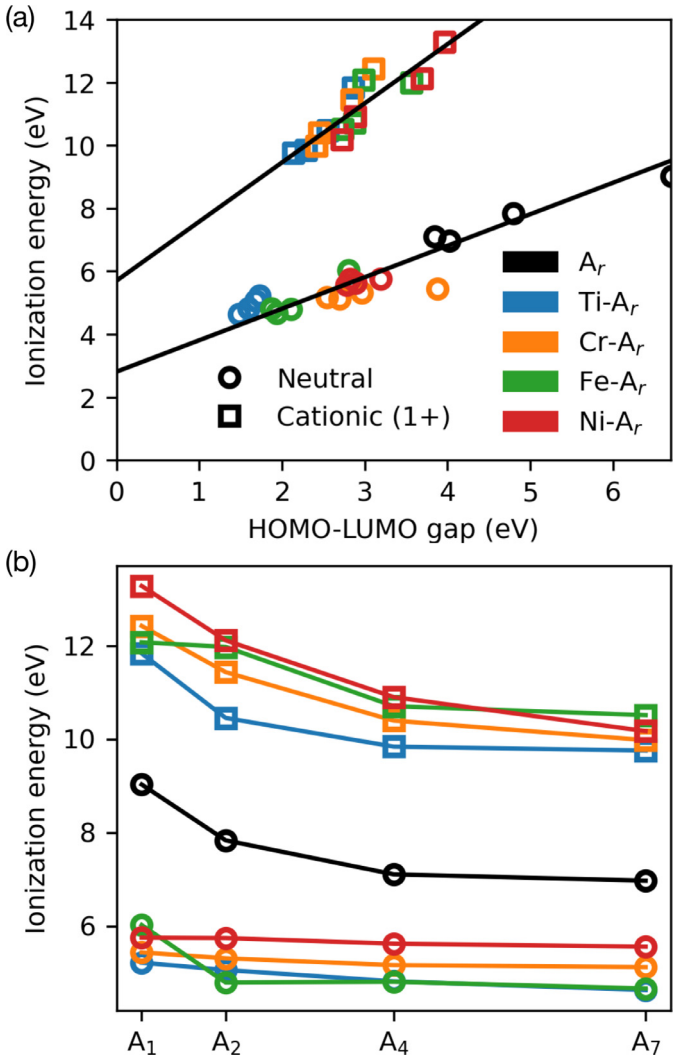

Fig. 6. (a) Correlation of adiabatic ionization energy with HOMO-LUMO gap. (b) Variation of adiabatic ionization energy of neutral and 1+ cationic complexes with number of aromatic rings.

Our computed binding energies of M-A_r^{2+} complexes with respect to dissociation to M^{2+}+A_r^0 are in reasonable agreement with literature computed values, as presented in Table 2. Good agreement is observed with additional results from Kolakkandy et al. [49] (not listed in Table 2). It is important to note that all previously reported binding energies [49,75,85] are based on the assumption of preserved multiplicity with M^{2+}+A_r^0 as the dissociated products. Nevertheless, an interesting question about these binding energies concerns the assignment of the dissociation products. In fact, all of the 2+ cationic complexes have a negative binding energy if M^{1+}+A_r^{1+} is assigned as the products, indicating that thermodynamically such complexes are unfavorable. To examine the energetics of the 2+ cationic complexes, we plot, as examples, the relative energies of the Ti-A_2^{2+} and Cr-A_2^{2+} complexes and their dissociated products in Fig. 4. Clearly, the energy of M^{2+}+A_2^0 is significantly higher than that of M^{1+}+A_2^{1+}, owing to the large second ionization energy of the fourth-row transition metals (> 12.80 eV [86]). Additionally, the multiplicity of the ground state 2+ cationic complexes matches that of the 2+ metal cations themselves (i.e., triplet, quintet, quintet, triplet for Ti, Cr, Fe, Ni, respectively). Hence, as Fig. 4 shows, both Ti-A_2^{2+} and Cr-A_2^{2+} complexes can undergo electronic excitation, i.e., an increase in the multiplicity, followed by exothermic dissociation to M^{1+}+A_2^{1+} of the same, combined multiplicity. In the case of Ni (not shown), there is no such spin excitation, as both the ground state Ni^{2+}+A_r^0 and Ni^{1+}+A_r^{1+} assume the triplet state, and the 2+ cationic complex dissociates more favorably to Ni^{1+}+A_r^{1+} than to Ni^{2+}+A_r^0.

3.2. HOMO-LUMO energy gaps

The HOMO-LUMO energy gaps computed for the four aromatic compounds are listed in Table 3. The values are in close agreement with established literature values [38,40,94,95] and experiments [94,96]. For example, the HOMO-LUMO gap of naphthalene was calculated to be 4.79 eV, compared to 4.71 eV in a previous DFT study [38] and 4.74 eV in a time-dependent DFT (TDDFT) study [95]. Literature values for pyrene range from 3.78 eV in a DFT calculation [38], 3.75 and 3.51 eV in a TDDFT calculation [94], and 3.53 eV from experiment [96], all of which are compared reasonably well with our 3.84 eV. The experimental value for coronene is at 3.72 eV versus our 4.02 eV, consistent with the overestimation of the HOMO-LUMO gap of coronene by the B3LYP functional as reported by Menon et al. [76].

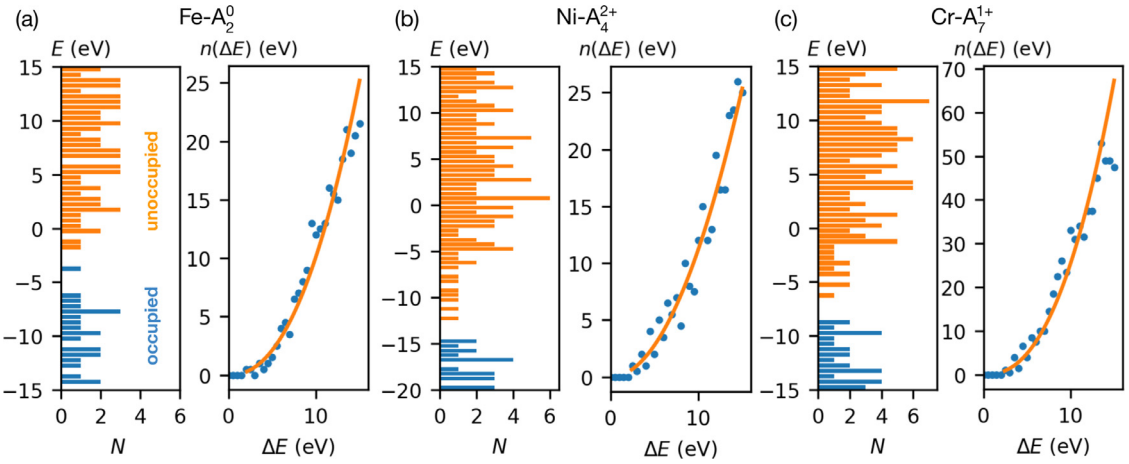

Fig. 7. Energy band structures of occupied and unoccupied energy states and possible number of energy-state transitions ($n(\Delta E)$) of selected metal-aromatic complexes. $N(E)$ refers to the density of a specific energy state at E. The line in each $n(\Delta E)$-vs.-ΔE plot corresponds to a Tauc-like fit, which yields the value of the power law exponent k.

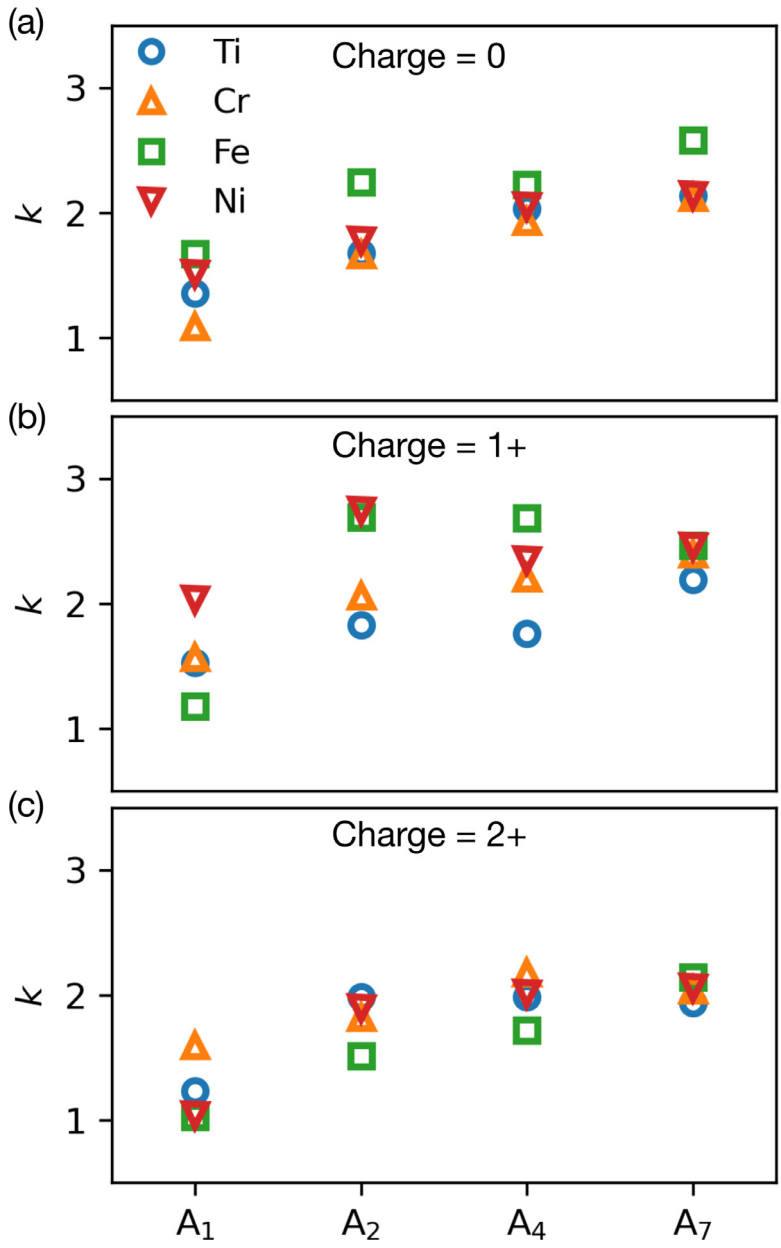

Fig. 8. Power law exponent k for (a) neutral, and (b) 1+ and (c) 2+ cationic metal-aromatic complexes.

Binding a metal atom with an aromatic affects its HOMO and LUMO electron densities significantly, as one would expect. The nature of the electronic excitation appears to be specific to a given metal-aromatic pair. For instance, Cr-A_r^0 complexes (in the septet state), have an electronic excitation with the ground state distributed in the aromatic and the excited state centered in the metal atom (Fig. 2(d) and supporting information); and such a lack of electronic density shared between the aromatic and the metal stems from the lack of electronic interaction between the metal and PAH, as confirmed by a NBO analysis. In contrast, Ti-A_r^0 and Fe-A_r^0 complexes involve non-local, coordination binding, and hence, the HOMO and LUMO molecular orbitals are distributed between the metal and the PAH π electrons. Ni-A_r^{2+} complexes (in the triplet state) exhibit a π to π^* excitation similar to PAHs without metal coordination. Clearly, the nature of the excitation and the change in the HOMO-LUMO gap depends on the nature of metal-aromatic binding, which in turn, depends on the charge state and system multiplicity.

The HOMO-LUMO gaps of the ground-state complexes are listed in Table 3 and compared in Fig. 5. In all cases, binding an aromatic with a metal results in appreciable reduction in its HOMO-LUMO gap, by more than 1 eV and in some cases up to 5 eV. For example, the HOMO-LUMO gap of the M-A_1^n complexes lies in the 1.7–4.2 eV range, a drop of >2 eV from that in benzene. M-A_2^n complexes have HOMO-LUMO gaps in the 1.7–3.7 eV range, metal-pyrene complexes have HOMO-LUMO gaps in the 1.6–2.9 eV range, and M-A_7^n complexes have HOMO-LUMO gaps smaller than 2.8 eV.

For neutral complexes, Ti has the strongest effect in reducing the energy gap, followed by Fe. Overall, Ni appears to have a weaker effect, except for the 2+ naphthalene and coronene complexes. The HOMO-LUMO gap of the 1+ complexes tends to be larger than that of neutral and 2+ complexes, with the exception of Cr complexes, whose HOMO-LUMO gap is largest in the neutral state. The effect of metal addition on HOMO-LUMO gap is more dramatic than the effect of PAH size or PAH dimerization. For instance, Ti addition decreases the band gap of benzene from

6.71 eV to 1.73 eV and that of coronene from 4.02 eV to 1.49 eV. A larger PAH with a comparable HOMO-LUMO gap is the considerably larger circum-3-coronene (1.5 eV), consisting of 61 aromatic rings [39]. As for dimerization, the stacking of two coronene molecules leads to a less than 10% decrease in HOMO-LUMO gap, which is again a small effect compared to metal addition. In larger clusters resembling CNPs, the smallest band gap component is expected to dominate and govern the band gap of the cluster and in the presence of metals, a metal-PAH aromatic complex will likely be that smallest band gap component [39].

We further notice that except for Ti-A_4^{1+} and Ti-A_7^{1+}, the HOMO-LUMO gap is greater than the binding energy for all complexes considered. Hence, photo-excitation can lead to complex dissociation. Interestingly, between the metal type and complex charge state, binding a metal with PAH can provide a versatile range of HOMO-LUMO energy gap values, and hence, it gives rise to the possibility of a tunable band gap for molecular electronics applications, as well as targeted organic plasmonic resonance utilization [97,98].

HOMO-LUMO gaps and ionization energies are well correlated, as shown in Fig. 6(a), for neutral and 1+ cationic complexes. This follows from Koopmans' theorem [99] and occurs because ionization energy is the sum of the HOMO-LUMO gap and the energy required to remove an electron from LUMO, or the Coulombic energy, which corresponds to the energy required to overcome the image charge effect. It is interesting to note that for the neutral species, the slope of the linear relation of Fig. 6(a) is roughly unity, with a 3 eV intercept that corresponds the Coulombic energy. For the 1+ cationic complexes, the slope is ≥ 2. Hence, in addition to the change in the HOMO-LUMO gap, aromatic molecule size impacts the Coulombic energy because of the effect of charge delocalization, as seen in Fig. 6(b). Benzene complexes have both the highest HOMO-LUMO gaps and largest Coulombic energies in general, while coronene complexes have the smallest HOMO-LUMO gaps and Coulombic energies.

3.3. Electronic transition

Electronic transition analysis is performed for each metal-aromatic complex of Table 3 in a manner similar to previous analyses of PAH clusters [31,40]. The results are illustrated in Fig. 7 for three example complexes. Here, the Kohn–Sham eigenvalues, which correspond to molecular orbital energies, are lumped in 0.5 eV bins and the resulting molecular orbital band structure is shown on the left-hand side plots of Fig. 7(a)–(c). The numbers of unoccupied and occupied orbital energies are used in Eq. (3) to obtain the number of possible transitions as a function of the transition energy. The number of transitions is plotted as on the right-hand side plots of Fig. 7(a)–(c). A Tauc-like power law fit is performed for the obtained data:

$$n(\Delta E) = A(\Delta E - E_{\text{H-L}})^k, \tag{4}$$

from which the value of the exponent k is extracted and plotted in Fig. 8 for all complexes considered. It is seen that the exponents k are around 2 for the metal-PAH complexes ($A_{\{2,4,7\}}$), which are close to the value measured for flame generated CNPs [31], and the theoretical values for a wide range of PAHs and PAH clusters [40]. The exponent k is between 1 and 2 for the M-A_1 complexes, but these k values are not as meaningful, because the small number of electronic states of M-A_1 complexes leads to a small number of available transitions, making the power law fit not as meaningful as in the case of multi-ring aromatics.

4. Conclusions

Molecular complexes of aromatics (benzene, naphthalene, pyrene, coronene) and fourth-row transition metals (Ti, Cr, Fe and Ni) are studied by density functional theory using the B3LYP functional with the triple-ζ cc-pVTZ basis set. The focus of the study was on the effect of metal bonding on the HOMO-LUMO gap of aromatics. Stable complexes were found from a comprehensive search over geometric consideration, charge state (0, 1+, and 2+), and spin multiplicities. The binding energies and HOMO-LUMO gaps of the ground-state complexes are calculated. The 2+ cationic complexes were determined to be thermodynamically unfavorable. Binding with a metal atom significantly lowers the HOMO-LUMO gap of the aromatic under all charge states. The number of possible transitions from occupied to unoccupied molecular orbitals in all metal-PAH complexes studied follow a power law relationship with respect to transition energy. Except for the benzene complexes, a power value was found to be close to those of PAH molecules and clusters without metal incorporation.

Declaration of Competing Interest

The authors declare that they have no known competing financial interests or personal relationships that could have appeared to influence the work reported in this paper.

Acknowledgments

This research was supported by the Air Force Office of Scientific Research under grant number FA9550-19-1-0261. Some of the computing for this project was performed on the Sherlock cluster at Stanford University. The authors thank Stanford University and the Stanford Research Computing Center for providing computational resources and support that contributed to these research results.

Supplementary material

The zero-point-corrected electronic energy is given for all converged structures and the HOMO and LUMO orbital energies for both α and β electrons, as well as the corresponding HOMO-LUMO gaps are given for all stable complexes. HOMO and LUMO orbital electron density plots are provided for all ground state complexes.

Supplementary material associated with this article can be found, in the online version, at doi:10.1016/j.combustflame.2022.112513

References

[1] H. Wang, Formation of nascent soot and other condensed-phase materials in flames, Proc. Combust. Inst. 33 (2011) 41–67.
[2] J.-B. Donnet, Carbon Black: Science and Technology, CRC Press, Boca Raton, Florida, 1993.
[3] C.A. Pope III, R.T. Burnett, G.D. Thurston, M.J. Thun, E.E. Calle, D. Krewski, J.J. Godleski, Cardiovascular mortality and long-term exposure to particulate air pollution: epidemiological evidence of general pathophysiological pathways of disease, Circulation 109 (2004) 71–77.
[4] J. Hansen, L. Nazarenko, Soot climate forcing via snow and ice albedos, Proc. Natl. Acad. Sci. 101 (2004) 423–428.
[5] B.S. Haynes, H.G. Wagner, Soot formation, Prog. Energy Combust. Sci. 7 (1981) 229–273.
[6] M. Frenklach, H. Wang, Detailed modeling of soot particle nucleation and growth, Symp. (Int.) Combust. 23 (1991) 1559–1566.
[7] H.F. Calcote, Mechanisms of soot nucleation in flames—A critical review, Combust. Flame 42 (1981) 215–242.
[8] K.H. Homann, Formation of large molecules, particulates and ions in premixed hydrocarbon flames; progress and unresolved questions, Symp. (Int.) Combust. 20 (1985) 857–870.
[9] M. Frenklach, H. Wang, Detailed mechanism and modeling of soot particle formation, Soot Formation in Combustion, Springer (1994), pp. 165–192.
[10] M. Frenklach, Reaction mechanism of soot formation in flames, Phys. Chem. Chem. Phys. 4 (2002) 2028–2037.
[11] A. D'Anna, Combustion-formed nanoparticles, Proc. Combust. Inst. 32 (2009) 593–613.
[12] B. Öktem, M.P. Tolocka, B. Zhao, H. Wang, M.V. Johnston, Chemical species associated with the early stage of soot growth in a laminar premixed ethylene-oxygen-argon flame, Combust. Flame 142 (2005) 364–373.

[13] Y. Bouvier, C. Mihesan, M. Ziskind, E. Therssen, C. Focsa, J.F. Pauwels, P. Desgroux, Molecular species adsorbed on soot particles issued from low sooting methane and acetylene laminar flames: a laser-based experiment, Proc. Combust. Inst. 31 (2007) 841–849.
[14] M.M. Maricq, An examination of soot composition in premixed hydrocarbon flames via laser ablation particle mass spectrometry, J. Aerosol Sci. 40 (2009) 844–857.
[15] K.O. Johansson, M.P. Head-Gordon, P.E. Schrader, K.R. Wilson, H.A. Michelsen, Resonance-stabilized hydrocarbon-radical chain reactions may explain soot inception and growth, Science 361 (2018) 997–1000.
[16] S.E. Stein, A. Fahr, High-temperature stabilities of hydrocarbons, J. Phys. Chem. 89 (1985) 3714–3725.
[17] J.P. Cain, P.L. Gassman, H. Wang, A. Laskin, Micro-FTIR study of soot chemical composition - evidence of aliphatic hydrocarbons on nascent soot surfaces, Phys. Chem. Chem. Phys. 12 (2010) 5206–5218.
[18] J.P. Cain, J. Camacho, D.J. Phares, H. Wang, A. Laskin, Evidence of aliphatics in nascent soot particles in premixed ethylene flames, Proc. Combust. Inst. 33 (2011) 533–540.
[19] B.D. Adamson, S.A. Skeen, M. Ahmed, N. Hansen, Detection of aliphatically bridged multi-core polycyclic aromatic hydrocarbons in sooting flames with atmospheric-sampling high-resolution tandem mass spectrometry, J. Phys. Chem. A 122 (2018) 9338–9349.
[20] M. Schenk, S. Lieb, H. Vieker, A. Beyer, A. Gölzhäuser, H. Wang, K. Kohse-Höinghaus, Imaging nanocarbon materials: soot particles in flames are not structurally homogeneous, ChemPhysChem 14 (2013) 3248–3254.
[21] A. Léger, J.L. Puget, Identification of the 'unidentified' IR emission features of interstellar dust? Astron. Astrophys. 137 (1984) L5–L8.
[22] L.J. Allamandola, A.G.G.M. Tielens, J.R. Baker, Polycyclic aromatic hydrocarbons and the unidentified infrared emission bands: auto exhaust along the Milky Way, Astrophys. J. 290 (1985) L25–L28.
[23] G.C. Sloan, T.L. Hayward, L.J. Allamandola, J.D. Bregman, B. DeVito, D.M. Hudgins, Direct spectroscopic evidence for ionized polycyclic aromatic hydrocarbons in the interstellar medium, Astrophys. J. 513 (1999) L65–L68.
[24] P. Marty, G. Serra, B. Chaudret, I. Ristorcelli, Iron-aromatics coordination in molecular clouds, Astron. Astrophys. 282 (1994) 916–923.
[25] A. D'Alessio, A. D'Anna, G. Gambi, P. Minutolo, The spectroscopic characterisation of uv absorbing nanoparticles in fuel rich soot forming flames, J. Aerosol Sci. 29 (1998) 397–409.
[26] P. Minutolo, G. Gambi, A. D'Alessio, The optical band gap model in the interpretation of the UV-visible absorption spectra of rich premixed flames, Symp. (Int.) Combust. 26 (1996) 951–957.
[27] M. Commodo, G. Tessitore, G. De Falco, A. Bruno, P. Minutolo, A. D'Anna, Further details on particle inception and growth in premixed flames, Proc. Combust. Inst. 35 (2015) 1795–1802.
[28] M. Commodo, G. De Falco, A. Bruno, C. Borriello, P. Minutolo, A. D'Anna, Physicochemical evolution of nascent soot particles in a laminar premixed flame: from nucleation to early growth, Combust. Flame 162 (2015) 3854–3863.
[29] M.L. Botero, E.M. Adkins, S. González-Calera, H. Miller, M. Kraft, PAH structure analysis of soot in a non-premixed flame using high-resolution transmission electron microscopy and optical band gap analysis, Combust. Flame 164 (2016) 250–258.
[30] J.H. Miller, J.D. Herdman, C.D. Green, E.M. Webster, Experimental and computational determinations of optical band gaps for PAH and soot in a N_2-diluted, ethylene/air non-premixed flame, Proc. Combust. Inst. 34 (2013) 3669–3675.
[31] C. Liu, A.V. Singh, C. Saggese, Q. Tang, D. Chen, K. Wan, M. Vinciguerra, M. Commodo, G. De Falco, P. Minutolo, A. D'Anna, H. Wang, Flame-formed carbon nanoparticles exhibit quantum dot behaviors, Proc. Natl. Acad. Sci. 116 (2019) 12692–12697.
[32] G. De Falco, G. Mattiello, M. Commodo, P. Minutolo, X. Shi, A. D'Anna, H. Wang, Electronic band gap of flame-formed carbon nanoparticles by scanning tunneling spectroscopy, Proc. Combust. Inst. 38 (2021) 1805–1812.
[33] S. Veronesi, M. Commodo, L. Basta, G. De Falco, P. Minutolo, N. Kateris, H. Wang, A. D'Anna, S. Heun, Morphology and electronic properties of incipient soot by scanning tunneling microscopy and spectroscopy, Combust. Flame 243 (2022) 111980.
[34] G.A. Kelesidis, S.E. Pratsinis, Soot light absorption and refractive index during agglomeration and surface growth, Proc. Combust. Inst. 37 (2019) 1177–1184.
[35] K. Wan, X. Shi, H. Wang, Quantum confinement and size resolved modeling of electronic and optical properties of small soot particles, Proc. Combust. Inst. 38 (2021) 1517–1524.
[36] E.M. Adkins, J.A. Giaccai, J.H. Miller, Computed electronic structure of polynuclear aromatic hydrocarbon agglomerates, Proc. Combust. Inst. 36 (2017) 957–964.
[37] E.M. Adkins, J.H. Miller, Towards a taxonomy of topology for polynuclear aromatic hydrocarbons: linking electronic and molecular structure, Phys. Chem. Chem. Phys. 19 (2017) 28458–28469.
[38] D. Chen, H. Wang, HOMO-LUMO energy splitting in polycyclic aromatic hydrocarbons and their derivatives, Proc. Combust. Inst. 37 (2019) 953–959.
[39] N. Kateris, A.S. Jayaraman, H. Wang, HOMO-LUMO gaps of large polycyclic aromatic hydrocarbons and their implication on the quantum confinement behavior of flame-formed carbon nanoparticles, Proc. Combust. Inst. (2022), doi:10.1016/j.proci.2022.07.168. In press.
[40] D. Chen, H. Wang, HOMO-LUMO gaps of homogeneous polycyclic aromatic hydrocarbon clusters, J. Phys. Chem. C 123 (2019) 27785–27793.
[41] M. Schenk, S. Lieb, H. Vieker, A. Beyer, A. Gölzhäuser, H. Wang, K. Kohse-Höinghaus, Morphology of nascent soot in ethylene flames, Proc. Combust. Inst. 35 (2015) 1879–1886.
[42] J.S. Fordyce, D.W. Sheibley, Estimate of contribution of jet aircraft operations to trace element concentration at or near airports, J. Air Pollut. Control Assoc. 25 (1975) 721–724.
[43] C.W. Bauschlicher Jr., H. Partridge, S.R. Langhoff, Theoretical study of transition-metal ions bound to benzene, J. Phys. Chem. 96 (1992) 3273–3278.
[44] C.W. Bauschlicher Jr., Fe^+- and Mg^+-polycyclic aromatic hydrocarbon complexes, Mol. Phys. 107 (2009) 809–818.
[45] A. Simon, C. Joblin, Thermochemistry and infrared spectroscopy of neutral and cationic iron-polycyclic aromatic hydrocarbon complexes of astrophysical interest: fundamental density functional theory studies, J. Phys. Chem. A 111 (2007) 9745–9755.
[46] C.-N. Yang, S.J. Klippenstein, Theory and modeling of the binding in cationic transition-metal-benzene complexes, J. Phys. Chem. A 103 (1999) 1094–1103.
[47] S.J. Klippenstein, C.-N. Yang, Density functional theory predictions for the binding of transition metal cations to pi systems: from acetylene to coronene and tribenzocyclyne, Int. J. Mass Spectrom. 201 (2000) 253–267.
[48] L. Senapati, S.K. Nayak, B.K. Rao, P. Jena, Atomic structure, binding energy, and magnetic properties of iron atoms supported on a polyaromatic hydrocarbon, J. Chem. Phys. 118 (2003) 8671–8680.
[49] S. Kolakkandy, S. Pratihar, A.J.A. Aquino, H. Wang, W.L. Hase, Properties of complexes formed by Na^+, Mg^{2+}, and Fe^{2+} binding with benzene molecules, J. Phys. Chem. A 118 (2014) 9500–9511.
[50] K. Ritrievi, J. Longwell, A. Sarofim, The effects of ferrocene addition on soot particle inception and growth in premixed ethylene flames, Combust. Flame 70 (1987) 17–31.
[51] J. Lahaye, S. Boehm, P. Chambrion, P. Ehrburger, Influence of cerium oxide on the formation and oxidation of soot, Combust. Flame 104 (1996) 199–207.
[52] A. Feitelberg, J. Longwell, A. Sarofim, Metal enhanced soot and PAH formation, Combust. Flame 92 (1993) 241–253.
[53] F. Zhang, C. Wang, J. Wang, S. Seifert, R.E. Winans, Soot formation and growth in toluene/ethylene combustion catalyzed by ruthenium acetylacetonate, Combust. Sci. Technol. (2021) 1–17.
[54] F. Zhang, C. Wang, W. Han, Y. Zou, J. Wang, S. Seifert, R.E. Winans, Soot formation and growth with palladium acetylacetonate-toluene injection in ethylene base flames investigated by in situ synchrotron small-angle X-ray scattering, Proc. Combust. Inst. 38 (2021) 1859–1866.
[55] X. Tang, C. Wang, F. Zhang, Q. Wang, J. Wang, S. Seifert, R.E. Winans, Effect of nickel acetylacetonate addition on soot inception and growth in an ethylene flame studied by using in situ small-angle X-ray scattering, Combust. Flame 206 (2019) 390–399.
[56] M. Wang, J. Mei, X. You, Effect of potassium chloride addition on soot formation during ethylene pyrolysis in a flow reactor, Combust. Flame 223 (2021) 118–126.
[57] Y. Du, P. Glarborg, W. Lin, Influence of potassium on benzene and soot formation in fuel-rich oxidation of methane in a laminar flow reactor, Combust. Flame 234 (2021) 111624.
[58] M. Wang, Y. Zhang, Y. Yu, W. Shan, H. He, Surface oxygen species essential for the catalytic activity of Ce–M–Sn (M = Mn or Fe) in soot oxidation, Catal. Sci. Technol. 11 (2021) 895–903.
[59] A.A. Khaskheli, L. Xu, D. Liu, Manganese oxide-based catalysts for soot oxidation: a review on the recent advances and future directions, Energy Fuel. 36 (2022) 7362–7381.
[60] G. Serra, B. Chaudret, Y. Saillard, A. Le Beuze, H. Rabaa, I. Ristorcelli, A. Klotz, Organometallic chemistry in the interstellar medium. I - Are organometallic reactions efficient processes in astrochemistry? Astron. Astrophys. 260 (1992) 489–493.
[61] P. Marty, P. de Parseval, A. Klotz, B. Chaudret, G. Serra, P. Boissel, Gas phase formation and reactivity of iron naphthylene cations: a route for polycyclic aromatic hydrocarbon growth, Chem. Phys. Lett. 256 (1996) 669–674.
[62] P. Marty, P. de Parseval, A. Klotz, G. Serra, P. Boissel, Organometallic reactions in the gas phase: measurements of the formation and dissociation rates of organometallic complexes, Astron. Astrophys. 316 (1996) 270–274.
[63] P. Cassam-Chenaı, Ab initio infra-red spectra of iron-polycyclic aromatic hydrocarbon compounds: a model case, Planet. Space Sci. 50 (2002) 871–876.
[64] H. Sun, J.H. Kramer, Perfluoroalkylated PAH *n*-type semiconductors: theory and experiment, New Fluorinated Carbons: Fundamentals and Applications, Progress in Fluorine Science Series, Elsevier (2017), pp. 155–176.
[65] X. Cui, C. Xiao, L. Zhang, Y. Li, Z. Wang, Polycyclic aromatic hydrocarbons with orthogonal tetraimides as *n*-type semiconductors, Chem. Commun. 52 (2016) 13209–13212.
[66] J.M. Farrell, C. Mützel, D. Bialas, M. Rudolf, K. Menekse, A.-M. Krause, M. Stolte, F. Würthner, Tunable low-LUMO boron-doped polycyclic aromatic hydrocarbons by general one-pot C-H borylations, J. Am. Chem. Soc. 141 (2019) 9096–9104.
[67] D.F. Perepichka, M.R. Bryce, Molecules with exceptionally small HOMO-LUMO gaps, Angew. Chem. Int. Ed. 44 (2005) 5370–5373.
[68] M.G. Wolfire, D. Hollenbach, C.F. McKee, A.G.G.M. Tielens, E.L.O. Bakes, The neutral atomic phases of the interstellar medium, Astrophys. J. 443 (1995) 152–168.
[69] M. Colket, J. Heyne, M. Rumizen, M. Gupta, T. Edwards, W.M. Roquemore, G. Andac, R. Boehm, J. Lovett, R. Williams, J. Condevaux, D. Turner, N. Rizk, J. Tishkoff, C. Li, J. Moder, D. Friend, V. Sankaran, Overview of the national jet fuels combustion program, AIAA J. 55 (2017) 1087–1104.

[70] A.D. Beck, Density-functional thermochemistry. III. The role of exact exchange, J. Chem. Phys 98 (1993) 5648–5652.
[71] C. Lee, W. Yang, R.G. Parr, Development of the Colle–Salvetti correlation-energy formula into a functional of the electron density, Phys. Rev. B 37 (1988) 785.
[72] P.J. Stephens, F.J. Devlin, C.F. Chabalowski, M.J. Frisch, Ab initio calculation of vibrational absorption and circular dichroism spectra using density functional force fields, J. Phys. Chem 98 (1994) 11623–11627.
[73] T.H. Dunning Jr., Gaussian basis sets for use in correlated molecular calculations. I. The atoms boron through neon and hydrogen, J. Chem. Phys. 90 (1989) 1007–1023.
[74] E.R. Davidson, Comment on "comment on dunning's correlation-consistent basis sets", Chem. Phys. Lett. 260 (1996) 514–518.
[75] B. Kerkeni, A.J.A. Aquino, M.R. Berman, W.L. Hase, Structures and binding energies for complexations of different spin states of Ni^{+} and Ni^{2+} to aromatic molecules, Mol. Phys. 117 (2019) 1392–1403.
[76] A. Menon, J.A.H. Dreyer, J.W. Martin, J. Akroyd, J. Robertson, M. Kraft, Optical band gap of cross-linked, curved, and radical polyaromatic hydrocarbons, Phys. Chem. Chem. Phys. 21 (2019) 16240–16251.
[77] M.J. Frisch, G.W. Trucks, H.B. Schlegel, G.E. Scuseria, M.A. Robb, J.R. Cheeseman, G. Scalmani, V. Barone, G.A. Petersson, H. Nakatsuji, X. Li, M. Caricato, A.V. Marenich, J. Bloino, B.G. Janesko, R. Gomperts, B. Mennucci, H.P. Hratchian, J.V. Ortiz, A.F. Izmaylov, J.L. Sonnenberg, D. Williams-Young, F. Ding, F. Lipparini, F. Egidi, J. Goings, B. Peng, A. Petrone, T. Henderson, D. Ranasinghe, V.G. Zakrzewski, J. Gao, N. Rega, G. Zheng, W. Liang, M. Hada, M. Ehara, K. Toyota, R. Fukuda, J. Hasegawa, M. Ishida, T. Nakajima, Y. Honda, O. Kitao, H. Nakai, T. Vreven, K. Throssell, J.A. Montgomery Jr., J.E. Peralta, F. Ogliaro, M.J. Bearpark, J.J. Heyd, E.N. Brothers, K.N. Kudin, V.N. Staroverov, T.A. Keith, R. Kobayashi, J. Normand, K. Raghavachari, A.P. Rendell, J.C. Burant, S.S. Iyengar, J. Tomasi, M. Cossi, J.M. Millam, M. Klene, C. Adamo, R. Cammi, J.W. Ochterski, R.L. Martin, K. Morokuma, O. Farkas, J.B. Foresman, D.J. Fox, Gaussian 16, 2016, Gaussian Inc., Wallingford CT.
[78] R.D. Johnson III (Ed.), NIST computational chemistry comparison and benchmark database, NIST standard reference database number 101, release 20, 2019, http://cccbdb.nist.gov.
[79] J.B. Foresman, Æ. Frisch, Exploring Chemistry with Electronic Structure Methods, third ed., Gaussian, Inc., Wallingford, CT, 2015, p. 440. 442–44, 454–56
[80] J.-L. Bredas, Mind the gap!, Mater. Horiz. 1 (2014) 17–19.
[81] J. Tauc, R. Grigorovici, A. Vancu, Optical properties and electronic structure of amorphous germanium, Phys. Status Solidi B 15 (1966) 627–637.
[82] P. Gori-Giorgi, A. Savin, Degeneracy and size consistency in electronic density functional theory, J. Phys. Conf. Ser. 117 (2008) 012017.
[83] R. Pandey, B.K. Rao, P. Jena, J.M. Newsam, Unique magnetic signature of transition metal atoms supported on benzene, Chem. Phys. Lett. 321 (2000) 142–150.
[84] F. Meyer, F.A. Khan, P.B. Armentrout, Thermochemistry of transition metal benzene complexes: binding energies of $M(C_6H_6)_x^+$ (x = 1, 2) for M = Ti to Cu, J. Am. Chem. Soc. 117 (1995) 9740–9748.
[85] C.A. Demircan, U. Bozkaya, Transition metal cation-π interactions: complexes formed by Fe^{2+}, Co^{2+}, Ni^{2+}, Cu^{2+}, and Zn^{2+} binding with benzene molecules, J. Phys. Chem. A 121 (2017) 6500–6509.
[86] Y. Ralchenko, A.E. Kramida, J. Reader, NIST ASD Team, NIST atomic spectra database (version 5.8), National Institute of Standards and Technology, Gaithersburg, MD (2020).
[87] D. Schröder, J. Loos, H. Schwarz, R. Thissen, D.V. Preda, L.T. Scott, D. Caraiman, M.V. Frach, D.K. Böhme, Single and double ionization of corannulene and coronene, Helv. Chim. Acta 84 (2001) 1625–1634.
[88] E. Clar, J.M. Robertson, R. Schlögl, W. Schmidt, Photoelectron spectra of polynuclear aromatics. 6. Applications to structural elucidation: "circumanthracene", J. Am. Chem. Soc. 103 (1981) 1320–1328.
[89] G.I. Nemeth, H.L. Selzle, E.W. Schlag, Magnetic ZEKE experiments with mass analysis, Chem. Phys. Lett. 215 (1993) 151–155.
[90] K.M. Wedderburn, S. Bililign, M. Levy, R.J. Gdanitz, Geometries and stabilities of 3D-transition metal-cation benzene complexes, $M^{+}Bz_n$ (M = Sc–Cu, n = 1, 2), Chem. Phys. 326 (2006) 600–604.
[91] T.D. Jaeger, D. van Heijnsbergen, S.J. Klippenstein, G. von Helden, G. Meijer, M.A. Duncan, Vibrational spectroscopy and density functional theory of transition-metal ion- benzene and dibenzene complexes in the gas phase, J. Am. Chem. Soc. 126 (2004) 10981–10991.
[92] T. Kurikawa, H. Takeda, M. Hirano, K. Judai, T. Arita, S. Nagao, A. Nakajima, K. Kaya, Electronic properties of organometallic metal- benzene complexes $[m_n(benzene)_m$ (m = Sc–Cu)], Organometallics 18 (1999) 1430–1438.
[93] J. Szczepanski, H. Wang, M. Vala, A.G.G.M. Tielens, J.R. Eyler, J. Oomens, Infrared spectroscopy of gas-phase complexes of Fe+ and polycyclic aromatic hydrocarbon molecules, Astrophys. J. 646 (2006) 666–680.
[94] M. Parac, S. Grimme, A TDDFT study of the lowest excitation energies of polycyclic aromatic hydrocarbons, Chem. Phys. 292 (2003) 11–21.
[95] G. Malloci, G. Mulas, G. Cappellini, C. Joblin, Time-dependent density functional study of the electronic spectra of oligoacenes in the charge states −1, 0, +1, and +2, Chem. Phys. 340 (2007) 43–58.
[96] J.B. Birks, Photophysics of Aromatic Molecules, Wiley Monographs in Chemical Physics, vol. 704, Wiley, New York, 1970.
[97] A. Manjavacas, F. Marchesin, S. Thongrattanasiri, P. Koval, P. Nordlander, D. Sanchez-Portal, F.J. García de Abajo, Tunable molecular plasmons in polycyclic aromatic hydrocarbons, ACS Nano 7 (2013) 3635–3643.
[98] A. Lauchner, A.E. Schlather, A. Manjavacas, Y. Cui, M.J. McClain, G.J. Stec, F.J. García de Abajo, P. Nordlander, N.J. Halas, Molecular plasmonics, Nano Lett. 15 (2015) 6208–6214.
[99] T. Koopmans, Über die Zuordnung von Wellenfunktionen und Eigenwerten zu den Einzelnen Elektronen Eines Atoms, Physica 1 (1934) 104–113.